Nanoscale deformation in polymers revealed by single-molecule super-resolution localization-orientation microscopy

Muzhou Wang,*[ab] James M. Marr,[cd] Marcelo Davanco,[c] Jeffrey W. Gilman,[b] J. Alexander Liddle[c]*

[a.] Department of Chemical and Biological Engineering, Northwestern University, Evanston, IL 60208. Email: mwang@northwestern.edu.

[b.] Materials Measurement Laboratory, National Institute of Standards and Technology, Gaithersburg, MD 20899.

[c.] Center for Nanoscience Science and Technology, National Institute of Standards and Technology, Gaithersburg, MD 20899. Email: liddle@nist.gov.

[d.] Maryland NanoCenter, University of Maryland, College Park, MD 20742.

Mechanical failure occurs through a hierarchical process, making it necessary to understand deformation at all length scales in order to develop advanced materials with, for example, enhanced toughness. This study addresses this challenge by demonstrating an optical imaging technique that detects damage at the nanoscale. We use single-molecule fluorescence microscopy experiments to simultaneously determine the position and orientation of single fluorophores from in-focus widefield images by fitting orientation-dependent point-spread functions determined by vectorial diffraction calculations. This capability is combined with switchable fluorophores in a single-molecule super-resolution microscopy scheme, enabling reconstruction of fluorophore orientation and alignment information at the nanoscale. We apply this method to polymer films deformed by thermal nanoimprint lithography, using fluorophore orientation mapping to detect areas of deformed material as small as 20 nm and distinguish them from neighboring, unperturbed regions. This technique advances the application of super-resolution microscopy in materials science, and may be applied to further the study of nanomechanical phenomena.

Mechanical failure in materials occurs over a range of length scales, down to that of an individual chemical bond.[1] The ability to visualize deformation at correspondingly small scales is essential to fully understand failure mechanisms. While several techniques can successfully characterize deformation at macroscopic length scales, nanoscale detection is still a significant challenge. For example, fluorescence techniques have a long history in the study of mechanical failure[2] and have been used for nearly a century in crack detection.[3] More recent work has relied on mechanochromic strategies, i.e., the introduction of fluorophores that detect deformation by switching into a bright state in response to strain.[4–7] This approach has led to significant advances in the past few years, providing insight into material behavior around crack tips, and suggesting design approaches that maximize strength and toughness.[8] However, the spatial resolution of fluorescence methods is typically limited by optical diffraction, preventing access to the nanometer length scale where mechanical failure begins. Other nanoscale techniques such as atomic force microscopy (AFM) or scanning/transmission electron microscopy (S/TEM) can visualize damage after the fact, but the evidence is typically indirect through imaging of nanostructural changes such as crazing fibrils. The sensitivity of polymeric materials to the electron beam presents additional challenges.

Conceptual Insight Statement

We demonstrate the detection of mechanical deformation in regions as small as 20 nm, using single-molecule super-resolution optical microscopy, through simultaneous measurement of fluorophore orientation and location. We apply this method to polymer films deformed by thermal nanoimprint lithography.

Current techniques for determining mechanical deformation have spatial resolution limited by optical diffraction (optical mechanochromism, birefringence, etc.) or use indirect methods of surveying damage post mortem (SEM, AFM, etc.). Our approach can non-invasively and directly detect nanoscale deformation using far-field optics. Detection of single-molecule orientation has been previously shown, but its combination with super-resolution microscopy for nanoscale orientation mapping has not been explored to our knowledge. The application to detecting damage in materials science is novel, and a large advance over existing research.

Detecting nanoscale deformation will significantly improve our understanding of macroscopic mechanical failure processes, which are the endpoint of hierarchical cascades that begin at the nanoscale. Scientists can use this information to design tough materials that delay the onset of mechanical failure. Additionally, while single-molecule super-resolution microscopy has had significant impact in the biological community, it is only now gaining a foothold in materials science. This study will further promote application of this technique to materials.

A method for directly detecting nanoscale deformation would greatly advance the understanding of mechanical failure and the development of strategies to mitigate it.

In this study, we demonstrate how single-molecule super-resolution microscopy can detect deformation by determining the position and orientation of single fluorophores: orientational alignment induced by mechanical strain can thus be mapped throughout a sample at the nanoscale. By circumventing the diffraction limit through a photoactivated localization microscopy (PALM) strategy, this technique can pinpoint regions of deformed material as small as 20 nm and resolve them from neighboring unperturbed areas.

Within the past decade, single-molecule super-resolution microscopy has become a standard technique for nanoscale structural characterization in the biological realm,[9–14] and is now transitioning into other applications such as materials science.[15–24] While many localization microscopy experiments fit single-emitter images to a 2D Gaussian to determine fluorophore position, more complex schemes, often requiring additional optics can encode further information such as orientation,[25–27] 3D position,[28–30] or emission spectra.[31,32] In this work, we fit the far-field radiation patterns of rotationally-fixed, in-focus fluorophores with vectorial diffraction calculations to determine single-molecule orientations without the need for additional optics. We then show that regions of relatively high fluorophore alignment correspond to regions that experienced mechanical strain, demonstrating that our technique can detect nanoscale deformation.
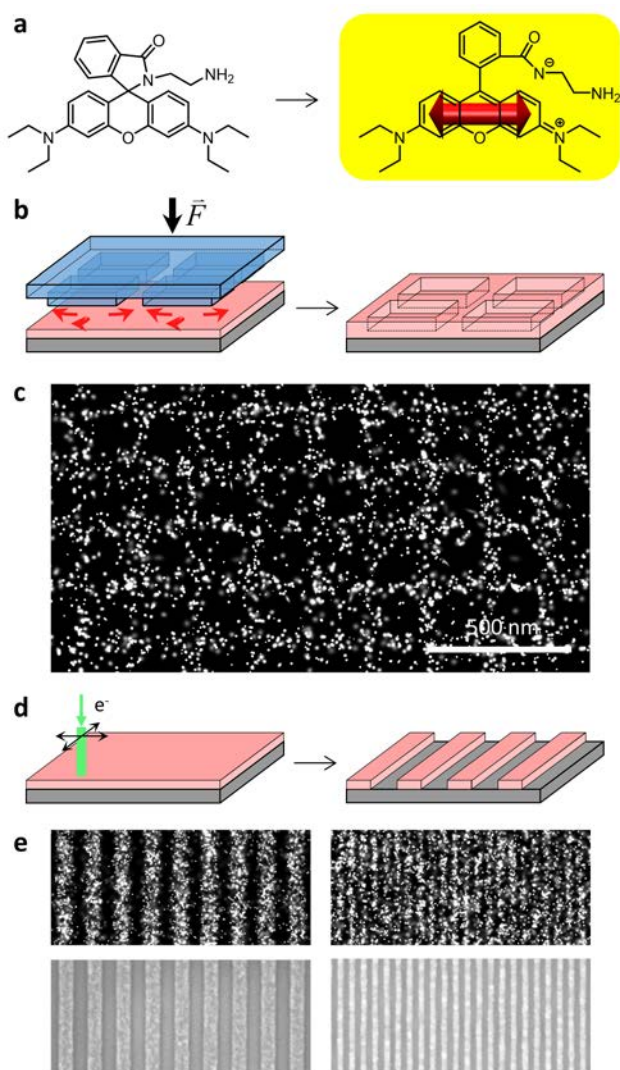
Figure 1. a) A rhodamine B spiroamide molecule undergoes a ring-opening isomerization upon UV exposure from a non-fluorescent state to a bright fluorescent isomer, enabling PALM imaging. The transition dipole moment is parallel to the xanthene ring system, as shown. **b)** When a rigid mold is heated and pressed into a PMMA resist layer in a thermal nanoimprint lithography process, the polymer experiences mechanical deformation and flow (red arrows in schematic). The mold was designed with periodic square protrusions (pitch of 200 nm, side of 140 nm, feature height of 60 nm), which form square wells in the PMMA layer (initial thickness of 40 nm) after nanoimprinting. **c)** Since the PMMA was doped with fluorophores before the fabrication process, single-molecule super-resolution microscopy reveals the thinned PMMA areas as squares that are sparsely-populated by fluorophores. **d)** Electron beam lithography is used to pattern 1:1 lines and spaces of 100 nm and 40 nm pitch in a 40 nm thick PMMA film. Mechanical deformation should be minimal in this process. **e)** Super-resolution microscopy (upper) is able to resolve these features, and comparison with scanning electron micrographs (lower) can establish resolution limits. The magnification is the same as in (c).

The effect of fluorophore orientation on far-field images has been widely explored in single-molecule experiments. A molecule's transition dipole moment vector causes anisotropic absorption/emission, which can be probed through illumination/detection dichroism[33] or photon collection and imaging. In many materials applications the mobility of fluorophores is minimal at typical experimental frame rates of milliseconds to seconds, so orientations can be considered

fixed. The in-focus or close-to-focus images of fixed single fluorophores can be non-centrosymmetric, resulting in orientation-dependent localization inaccuracies of > 50 nm in some cases, if simple Gaussians are fit to the true PSFs.[34,35] More sophisticated analysis schemes enable orientations of single fluorophores to be determined and used as a reporter of local material behavior. For example, fluorophores can align with polymer chains and thus probe relaxation dynamics,[36] At the single-molecule level, fluorescence polarization measurements can reveal the motion of single biomolecules,[37] or the macroscopic mechanical deformation of a polymer melt.[38] Direct analysis of individual widefield images,[26] or through various schemes including defocused imaging or additional optics,[27,39] can simultaneously determine the position and orientation of single fluorophores. However, we are unaware of any previous attempts to couple fluorophore orientation using PSF fitting with a switchable fluorophore in a PALM-type experiment. Such a scheme would generate super-resolved images, while simultaneously revealing the local nanoscale fluorophore orientation distribution.
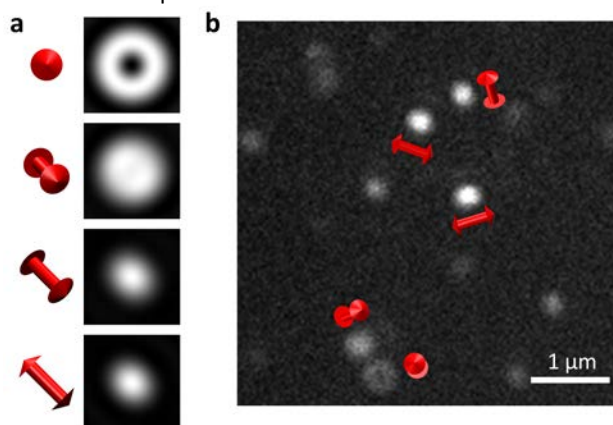

Figure 2. a) Images of point-spread functions (PSFs) calculated using a full vectorial diffraction model for a dipole emitter of λ = 580 nm in a dielectric medium of n = 1.5, imaged using an NA = 1.45 objective. From top to bottom, polar angles are 90° (perpendicular to optical axis), 60°, 30°, and 0°. Each emitter has an azimuthal angle of 45° between the vertical and horizontal axes. Dipole orientations are indicated by the double-headed red arrows. The length of one side of each image is 600 nm. **b)** Image of single fluorophores from a typical experiment. By fitting the PSF model to the images, we assigned dipole orientations (red arrows) as shown for the 5 representative molecules.

We demonstrate such a capability by determining the areas of mechanical deformation in a polymer film patterned by thermal nanoimprint lithography (Fig. 1).[40] We expected that the deformations from the imprint process would appear as locally-nonuniform fluorophore orientation distributions.[41] A rigid mold with periodic square protrusions of 200 nm pitch and equal protruding and non-protruding area was heated and pressed into a poly(methyl methacrylate) (PMMA, 950 kg/mol) film doped with a photoactivatable rhodamine spiroamide fluorophore (Fig. 1a), producing square wells (Fig. 1b) that we imaged using PALM (Fig. 1c). We determined that our system had sufficient spatial resolution to detect the deformed areas, by performing control experiments on similar films patterned by electron-beam lithography (see Supporting Information), which we do not expect to perturb fluorophore orientations (Fig. 1d). Line-space patterns were chosen because they can be easily compared to ground-truth data generated by top-down SEM. These patterns can be resolved by super-resolution

imaging down to 20 nm half-pitch features (Fig. 1e), but further analysis was performed to determine the localization uncertainty of each fluorophore, which defines the ultimate resolution limit. The average localization uncertainty is calculated by first producing one-dimensional intensity profiles by integrating the super-resolution images along the lines. This generates well-sampled data and largely eliminates errors from insufficient labelling density, combining >10^5 localization events into a single profile. These profiles are then fit to a square wave, representing the ground-truth structure, convolved with a Gaussian of variance σ^2, representing the average localization uncertainty. Best fits were found at σ = 8.2 nm (Fig. S1c), implying that on average, the location of each individual fluorophore can be determined to within this value. Contributions to this localization uncertainty are discussed at length in the Supporting Information.

We determine fluorophore orientations by fitting model point-spread functions (PSFs) derived from vectorial diffraction calculations to the experimental widefield images. The fitting procedure uses maximum likelihood estimation (MLE) of fluorophore intensity, x- and y-positions, azimuthal (in-plane, α) and polar (out-of-plane, β) angles with respect to the optic axis, and background intensity. Positions and orientations of each fluorophore are thus determined. The fluorophores are physically mixed with PMMA, whose glassy state at room temperature holds the positions and orientations fixed on the experimental time scale. The PMMA-dye mixture (n = 1.491) is deposited on a coverslip (n = 1.515), and then covered with a drop of glycerol (n = 1.473). This degree of index matching ensures that the PSFs for all orientations are approximately centrosymmetric around the true fluorophore position (Fig. 2a), reducing localization inaccuracies. The polar angle determines the spatial extent of the PSF, where the most sharply-peaked pattern occurs when the transition dipole moment is exactly in-plane. The PSF becomes more spread out as the angle with the optical axis decreases, and the pattern reaches a rotationally-symmetric "doughnut" shape when the transition moment vector points exactly out-of-plane. The azimuthal angle is encoded as a slight elongation of the PSF, which becomes more pronounced for orientations that are more in-plane, when the polar angle approaches 90°. In a typical frame, the positions and orientations can be assigned for all the observed single molecules (Fig. 2b).

Agreement between the calculated and the experimentally-observed PSFs are excellent even for the brightest fluorophores (Fig. 3a), where shot noise effects are minimized and thus the shape of the two PSFs are most easily compared. To rigorously determine if the calculated PSF agrees with the experimentally observed radiation patterns, we calculated a pixel-by-pixel z-score, $z = \left(m_{\exp} - m_{calc} \right) / \sqrt{m_{calc}}$, where m_{exp} is the number of experimentally-observed photons and m_{calc} is calculated from the model PSF, which serves as both the mean and variance of the Poisson-distributed shot noise. The z-scores of each pixel plotted as an image show little discernable pattern, suggesting that the model fits with minimal systematic error. Fits to a series of images of a persistent, bright fluorophore enable direct measurement of the precision of the determined positions and orientations, in comparison to the calculated Cramer-Rao lower bound (CRLB) derived from the MLE analysis (Fig. 3b). The standard deviation of the difference in x-positions between successive frames comes within 2% of

the CRLB, while the azimuthal and polar angle precisions are 38% and 19% larger than the respective CRLB values. The calculated PSFs are thus a good approximation to the single-molecule images, and enable orientations to be determined with precisions consistent with the CRLB.

In addition to the precision of determining fluorophore orientation, it is also necessary to verify the accuracy of our PSF fitting scheme.[42,43] This is not straightforward, because ground truth measurements of known molecular orientation are difficult. We make progress here for azimuthal orientation since the transition dipole moments $\vec{\mu}$ for absorption and emission are parallel, because the fluorophores are spatially fixed on experimental time scales. Since the probability of absorption is $P_{abs} \propto \left(\vec{\mu} \cdot \vec{E} \right)^2$, where $\vec{E}$ is the electric field vector of the incident radiation, this means that a fluorophore oriented approximately parallel to the y-axis should absorb more light, and thus appear brighter, when illuminated with y-polarized light compared to x-polarized light, and *vice versa*. The ratio in apparent brightness of a fluorophore under y- versus x-polarized illumination should be tan$^2\alpha$, where α is the azimuthal angle of the dipole moment with respect to the +x axis. The high numerical aperture objective in this experiment does not substantially alter the polarization because we illuminate the field of view with collimated light in a widefield configuration.[44,45] Repeated switching of the incident polarization on persistently fluorescent molecules enables comparison of the α determined from PSF fitting with the observed brightness ratio for the two incident polarizations (Fig. 3c). This procedure for verifying accuracy is not well-suited for systematic study, as most molecules are only fluorescent for a few frames, and molecules may also spontaneously switch into brighter or darker states during the measurement. However, the brightness ratios are consistent with PSF fitting results for
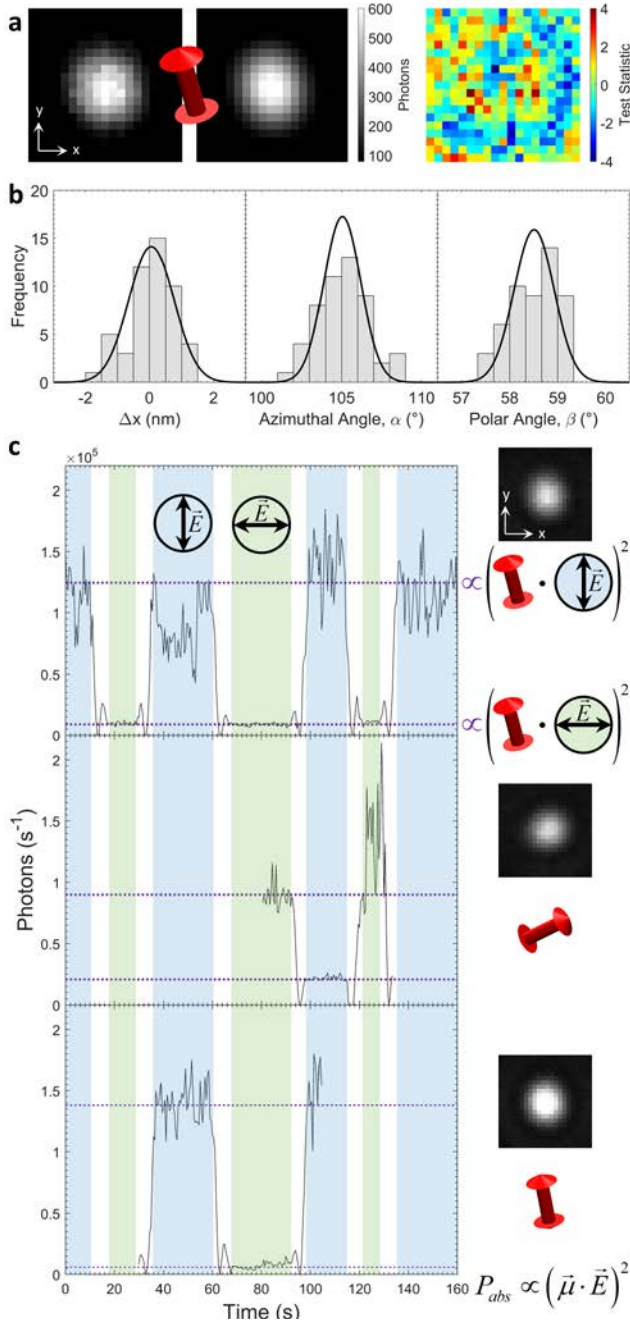
Figure 3. a) An experimentally-acquired single-molecule image (left) was fit by MLE to determine a total photon count of 4.1×10^4, azimuthal angle of 16° counter-clockwise from the +y axis, and polar angle of 58° from the optical axis. A simulated PSF (middle) with the same parameters is also shown. The image is 29 × 29 pixels, with a measured pixel size of 32.2 nm. A z-test statistic was calculated for each pixel (right), as discussed in the main text. **b)** Histograms of 50 repeated measurements of the fluorophore shown in (a) of the difference in x-positions between successive frames, the azimuthal angle, and the polar angle. The standard deviations of these measurements were 0.72 nm, 1.6°, and 0.50° respectively. Also shown are expected Gaussian distributions based on root-mean-squared CRLBs derived from the MLE fits, which were 0.71 nm, 1.2°, and 0.42°. Each frame had a similar photon count and was acquired every 0.5 s. **c)** Fluorophores are alternately illuminated with x- (green) and y-polarized (blue) light. The fluorescence output of three molecules is plotted vs. time, and their corresponding images are shown (right). This brightness changes depending on the alignment between the transition dipole and the incident electric field. Azimuthal angles relative to the +x axis determined by PSF fitting are 105°, 25.6°, and 101° for the three molecules from top to bottom, as illustrated by the red arrows. Horizontal dotted lines (violet) indicate the expected brightnesses proportional to $\left(\vec{\mu} \cdot \vec{E}\right)^2$.

several randomly chosen molecules, providing evidence that our azimuthal orientation estimates from PSF fitting are both precise and accurate.

Because our method uses in-focus images to determine orientation, the signal from each fluorophore is spread over a minimal diffraction-limited number of pixels. Combination with well-established single-molecule super-resolution strategies, where many switchable fluorophores are in their bright states in a single camera frame, is thus straightforward. The small spatial extent of each molecule's PSF minimizes overlap between images from nearby emitters, and the position and orientation of each molecule can be simultaneously determined. In the super-resolution image of the polymer film deformed by nanoimprint lithography (Fig. 1b), each localization event is thus assigned an azimuthal orientation determined by PSF fitting. The resulting information can be combined into a spatial map of fluorophore orientation and alignment throughout the nanostructure. For most PALM experiments, which only use fluorophore positions, an image is rendered by representing each localization event as a Gaussian whose σ is the CRLB localization precision, and the final image is the sum of all events. For the experiments described here, orientation distributions can be plotted analogously. Events are represented in the angular domain as von Mises distributions centered at the determined azimuthal angle, with a dispersion parameter κ related to the angular CRLB precision σ_{angle} by the

equation $I_1\left(\kappa\right)/I_0\left(\kappa\right) = e^{-\sigma_{angle}^2/2}$, where I_n is a modified Bessel function of the first kind, of order n.

To explore orientation distributions at various positions within the nanoimprinted square wells (Fig. 1b), we first combine events from many identical wells from a large field of view (Fig. S6) into a single unit cell of the array to effectively increase the labelling density and improve statistics. At every point within the unit cell, we render an azimuthal orientation distribution by summing nearby events according to a Gaussian kernel with σ = 15 nm. These distributions determine a two-dimensional order parameter throughout the well, shown in Fig. 4a. The order parameter is given by,

$$S = \left\langle 2\cos^2\theta - 1 \right\rangle, \tag{1}$$

where ϑ is the difference between the local mean angle and angles within the distribution. The fluorophore orientations are distributed predominantly uniformly throughout the well as shown by the low order parameter, but there is a preference for horizontal alignment along the north wall (+y region). Although the order parameter is relatively low, we can demonstrate that the alignment is statistically significant and indeed arises from the mechanical deformation. The statistical significance is determined by performing a Rayleigh test for angular uniformity. The test statistic is given by,

$$z = nS^2, \tag{2}$$

where n is the number of angles in the distribution, and $2z$ follows a χ^2 distribution with two degrees of freedom when $n > 100$, which is true in this experiment. Thus, the null hypothesis that the orientations are uniform is rejected with 95 % confidence when $z > 3.00$. Regions of relatively high S near the center of the well (center of Fig. 4a) have statistically uniform orientations since there are fewer localization events (small n) because the film is thinner. The alignment is significant only along the north wall (Fig. 4b), and further demonstrated by the orientation distributions from three selected locations (Fig. 4c).
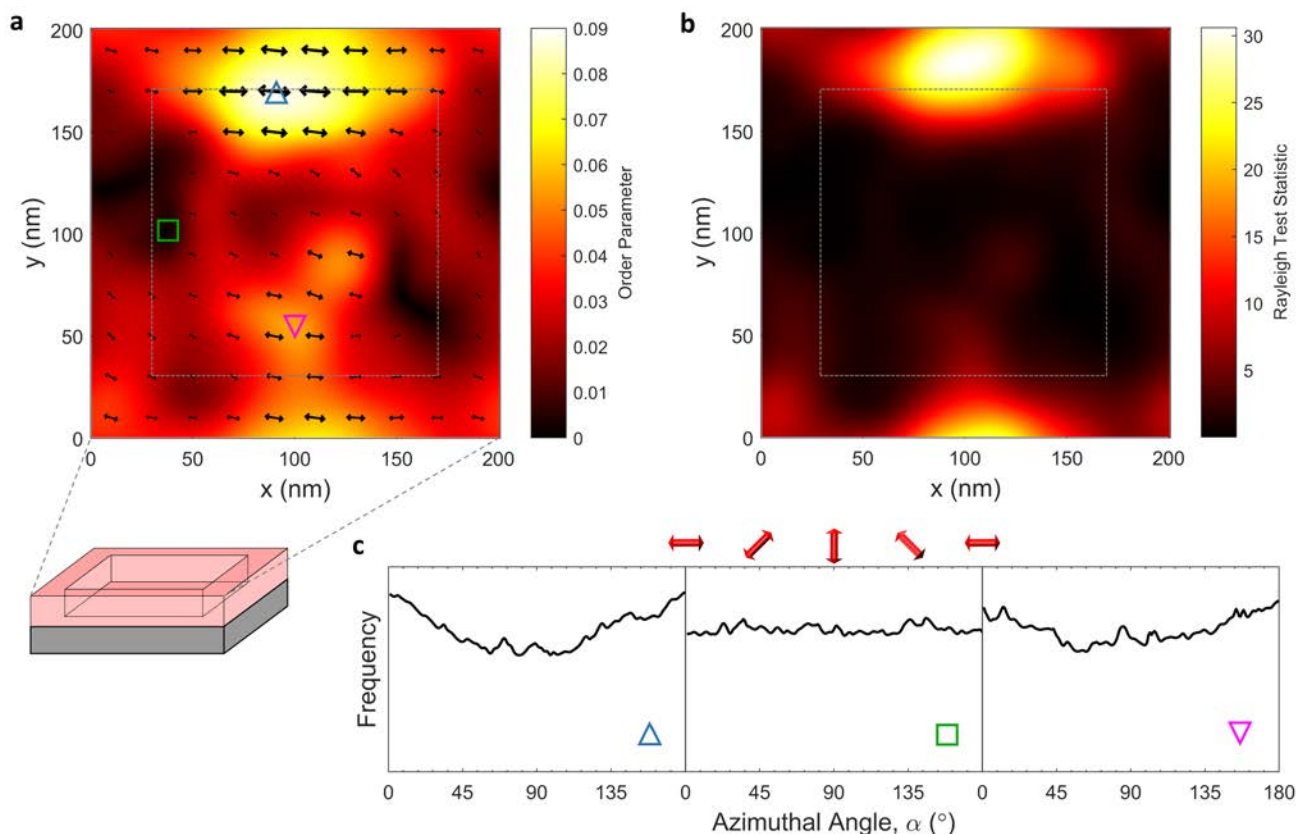
Figure 4. a) The distribution of fluorophore orientations across a nanoimprinted square well, as shown in the inset schematic. Information from fluorophore positions and orientations was combined from 1300 wells identical to the ones shown in Fig. 1c. The result is a single unit cell with an effective labelling density of ≈ 1 to 4 fluorophores per nm^2 (Fig. S7). After applying a smoothing Gaussian kernel with $\sigma = 15$ nm, azimuthal orientation distributions are determined at every point within the periodic wells and used to calculate a two-dimensional order parameter (see text). The orientation of the arrows indicates the mean direction, while the length and thickness of the lines together with the color map indicate the magnitude of the order parameter. The gray dotted box indicates the position of bottom of the well: inside the box the film is 10 nm thick and outside it is 70 nm thick. **b)** The corresponding spatial variation of the Rayleigh test statistic (see text). The statistical significance of the order parameter is tested against a null hypothesis of uniformly distributed orientations. The null hypothesis is rejected with 95 % confidence when the test statistic is above 3.00. The gray dotted box again denotes the well, as was shown in (a). **c)** The orientation distributions at the positions indicated by the corresponding triangle, square, and inverted triangle in (a). Consistent with (a) and (b), the distribution deviates most significantly from random at the north (+y) edge.

We explain this alignment phenomenon by examining the fabrication process. Previous work has identified residual stresses from the imprint process throughout the nanopatterns,[46] that presumably manifest in non-equilibrium conformations of the polymer chains. Although we expected that these deformations would induce nonuniform fluorophore orientation throughout the structure, it is likely that the high temperatures during imprint lead to the rapid orientational randomization of the fluorophores, which are both significantly smaller than the polymer chains and not entangled. However, separation of the rigid mold from the polymer film is performed at room temperature, which is deep in the glassy regime for PMMA. Because the separation always requires peeling that is initiated from one side, the features of the mold are removed at an angle which induces plastic deformation and damage along one side of the wells (Fig. 5a). The location of the alignment phenomenon is always consistent with the peeling direction. Our proposed mechanism is further supported by AFM, which shows protruding features at the north (+y) side of each well, corresponding to the aligned region identified by super-resolution orientation microscopy (Fig. 5bc). These features rest on top of unperturbed material, so the orientation distributions in this region contain aligned fluorophores in the sheared features in addition to the randomly oriented

fluorophores in the underlying region. This random component causes the order parameter to never exceed 0.1.

The excellent agreement between the protruding regions determined by AFM and the regions of high order parameter determined by optical microscopy suggest that super-resolution orientation microscopy can detect mechanical deformation at the nanoscale. The deformed regions are only ≈ 20 nm in width and thus far below the optical diffraction limit, but are distinguishable from neighboring undeformed regions at the east and west sides and bottom of each well that are less than 200 nm away. These undeformed areas provide useful internal controls to our experiment, as they do not show significant alignment in the fluorophore orientation distributions. Multiple tests under these conditions have demonstrated that this phenomenon is highly reproducible (Fig. S8), while detailed modeling indicates that it is not an artifact due to the slight deviations from perfect index matching (Figs. S9 and S10). These controls confirm that the observed orientational alignment arises definitively from the mechanical deformation introduced during the nanofabrication process.

To our knowledge, this is the first demonstration of super-resolution orientation microscopy to reveal deformation and damage at the nanoscale. Although this particular deformation was verified by other techniques, AFM only provided indirect evidence through the visible structural changes caused by the
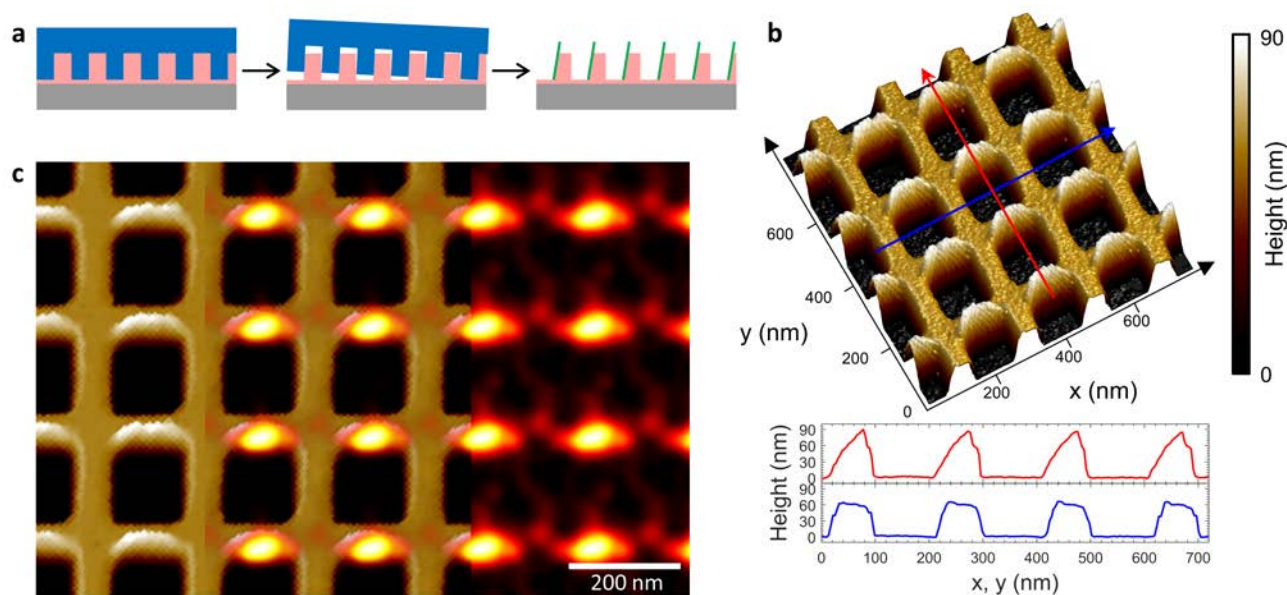
Figure 5. a) The rigid mold is removed from the PMMA film below T_g by peeling from one side, causing plastic deformation. This results in a damage zone indicated by green. **b)** This is confirmed by atomic force microscopy, where the line trace along y (red) shows features protruding 25 nm above the north $(+y)$ wall of each well. Minimal protrusions are shown in the line trace along x (blue). **c)** Composite of the AFM image and the Rayleigh test statistic data tiled from Fig. 4b, where the two representations are superimposed in the middle. The excellent correlation between the protruding regions detected by AFM and the ordered (bright) regions determined *via* super-resolution orientation microscopy suggests that fluorophore orientation measurements can clearly identify nanoscale deformation.

mechanical strain. Super-resolution orientation directly probes fluorophore alignment which is sensitive to the underlying molecular structure in the damaged regions. For samples in which structural changes are less obvious, such as features buried underneath a surface, or at the initial onset of damage, our technique offers a significant advantage.

Conclusions

In summary, we perform single-molecule super-resolution microscopy on in-focus, index-matched polymer films using normal widefield optics, where fluorophores are spatially fixed by the surrounding matrix. Each fluorophore image is fit to calculated point-spread functions that enable simultaneous determination of molecular position and orientation of the transition dipole moment. After quantifying the precision and accuracy of our fits, we apply our technique to films deformed by nanoimprint lithography, revealing nanoscale regions of anisotropic orientation distributions that are signatures of mechanical deformation. This approach may enhance the already intense interest in the materials community in optical detection of mechanical processes by enabling access to the nanoscale, where many of these phenomena originate.[47,48] As super-resolution microscopy is applied to problems beyond the biological space, the use of fluorophore orientation to probe nanomechanics provides a new tool to study nanostructured systems for the broader scientific community.

Experimental section

Image fitting and rendering. The positions and orientations of single fluorophores were determined from their raw images by maximum likelihood estimation (MLE) using theoretical orientation-dependent point-spread functions (PSFs). The custom code was adapted from and combined aspects from various sources.[26,49,50] Briefly, segmented images of single molecules were fit to parameters of intensity, position (x, y), azimuthal angle (α), polar angle (β), and background. The theoretical PSFs were calculated on-the-fly after pre-calculating and storing the various functions and normalization constants for the isotropic PSF component, orthogonal PSF component, etc. Expected photon counts were calculated by integrating the theoretical PSF over the area of each pixel in the segmented image, and the overall likelihood function based on Poisson statistics was maximized by Newton's method. Multiple emitters in a segmented image were handled by simply including intensity, position, and orientation parameters for additional fluorophores in the MLE fit, and the maximum number of emitters attempted was two. Quality of fit was determined using a χ^2 test as previously described.[50] Emitters were rejected for various reasons such as insufficient photon count, positions too close to the edge of segmented image, failing the χ^2 test, etc. The final emitter positions were corrected for lateral drift using fiducial markers, and then rendered as a normalized 2D Gaussian with a covariance matrix given by the Cramer-Rao lower bound of the position parameters. Further details may be found in the Supporting Information.

Nanoimprint lithography. To fabricate the nanoimprint mold, a hydrogen silsesquioxane solution in methyl isobutyl ketone was spin-coated on a Piranha-cleaned silicon wafer and then baked at 100 °C for 5 min, for a final thickness of 60 nm. Square protrusions of side length 140 nm, regularly spaced at 200 nm pitch, were written onto the wafer as described above, with an areal dose of 25 mC·cm-2. The features were developed by soaking the wafer in an aqueous solution of sodium hydroxide at mass fraction 1 % and sodium chloride at mass fraction 4 % for 4 min,[51] and then verified by SEM. Prior to nanoimprinting, the mold was coated with a non-adhesion layer by soaking in a solution of 1 % by mass (tridecafluoro-1,1,2,2-tetrahydrooctyl)dimethylchlorosilane in toluene overnight.

Dye-doped polymer films were prepared by spin-coating a solution of mass fraction 0.1 % rhod-butyl relative to PMMA 950k in anisole onto Piranha-cleaned No. 1.5 glass coverslips. The films were baked at 180 °C for 5 min, and the thickness was 40 nm. The features on the mold were transferred to the polymer film by nanoimprint lithography as follows. The mold and film were placed in vacuum, compressed together at 2.76 MPa (400 psi), and heated to 80 °C for 6 min. After cooling to room temperature, they were then separated using a razor blade in a direction parallel to the features. Since the total protruding and non-protruding areas of the mold were equal, the thickness of the side of each well was 70 nm, and the thickness of the residual layer at the center of each well was 10 nm. The features were examined by atomic force microscopy in peak force tapping mode. Scans were performed at a 45° angle to the main features, and the trace and retrace signals were perfectly superimposable. The same film was then imaged by single-molecule microscopy (see Supporting Information).

Conflicts of interest

There are no conflicts to declare.

Acknowledgements
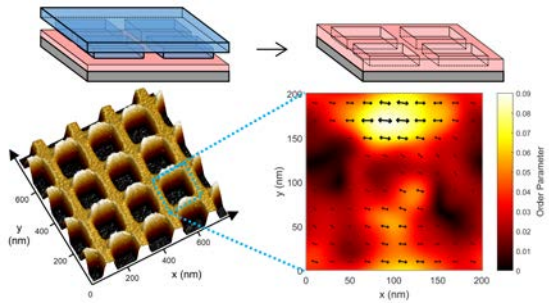
Supporting information

Discussion of localization uncertainty, PSF fitting. PSF fitting code. Experimental methods for synthesis of the fluorophores and polymers, and electron beam lithography. Single-molecule microscopy apparatus, Rendered super-resolution image of the total nanoimprint experiment area, localization event density, and optical simulations of PSFs.

References

(1)   Creton, C.; Ciccotti, M. Fracture and Adhesion of Soft Materials: A Review. *Reports Prog. Phys.* **2016**, *79*, 046601.

(2)   Lake, G. J.; Thomas, A. G. The Strength of Highly Elastic Materials. *Proc. R. Soc. London Ser. A Math. Phys. Sci.* **1967**, *300* (1460), 108–119.

(3)   Switzer, R. C. Flaw Detection. 2,259,400, 1941.

(4)   Calvino, C.; Neumann, L.; Weder, C.; Schrettl, S. Approaches to Polymeric Mechanochromic Materials. *J. Polym. Sci. Part A Polym. Chem.* **2017**, *55* (4), 640–652.

(5)   Black, A. L.; Lenhardt, J. M.; Craig, S. L. From Molecular Mechanochemistry to Stress-Responsive Materials. *J. Mater. Chem.* **2011**, *21* (6), 1655–1663.

(6)   Caruso, M. M.; Davis, D. A.; Shen, Q.; Odom, S. A.; Sottos, N. R.; White, S. R.; Moore, J. S. Mechanically-Induced Chemical Changes in Polymeric Materials. *Chem. Rev.* **2009**, *109*, 5755–5798.

(7)   Suhina, T.; Weber, B.; Carpentier, C. E.; Lorincz, K.; Schall, P.; Bonn, D.; Brouwer, A. M. Fluorescence Microscopy Visualization of Contacts between Objects. *Angew. Chemie - Int. Ed.* **2015**, *54* (12), 3688–3691.

(8)   Zhao, X. Designing Toughness and Strength for Soft Materials. *Proc. Natl. Acad. Sci.* **2017**, *114* (31), 201710942.

(9)   Huang, B.; Bates, M.; Zhuang, X. W. Super-Resolution Fluorescence Microscopy. *Annu. Rev. Biochem.* **2009**, *78*, 993–1016.

(10)   Betzig, E.; Patterson, G. H.; Sougrat, R.; Lindwasser, O. W.; Olenych, S.; Bonifacino, J. S.; Davidson, M. W.; Lippincott-Schwartz, J.; Hess, H. F. Imaging Intracellular Fluorescent Proteins at Nanometer Resolution. *Science* **2006**, *313* (5793), 1642–1645.

(11)   Sahl, S. J.; Moerner, W. E. Super-Resolution Fluorescence Imaging with Single Molecules. *Curr. Opin. Struct. Biol.* **2013**, *23* (5), 778–787.

(12)   Hell, S. W.; Sahl, S. J.; Bates, M.; Zhuang, X.; Heintzmann, R.; Booth, M. J.; Bewersdorf, J.; Shtengel, G.; Hess, H.; Tinnefeld, P.; Honigmann, A.; Jakobs, S.; Testa, I.; Cognet, L.; Lounis, B.; Ewers, H.; Davis, S. J.; Eggeling, C.; Klenerman, D.; et al. The 2015 Super-Resolution Microscopy Roadmap. *J. Phys. D. Appl. Phys.* **2015**, *48* (44), 443001.

(13)   Thompson, M. A.; Lew, M. D.; Moerner, W. E. Extending Microscopic Resolution with Single-Molecule Imaging and Active Control. *Annu. Rev. Biophys.* **2012**, *41*, 321–342.

(14)   Xu, K.; Zhong, G. S.; Zhuang, X. W. Actin, Spectrin, and Associated Proteins Form a Periodic Cytoskeletal Structure in Axons. *Science* **2013**, *339* (6118), 452–456.

(15)   Nevskyi, O.; Sysoiev, D.; Oppermann, A.; Huhn, T.; Wöll, D. Nanoscopic Visualization of Soft Matter Using Fluorescent Diarylethene Photoswitches. *Angew. Chemie Int. Ed.* **2016**, *55*, 12698–12702.

(16)   Siemes, E.; Nevskyi, O.; Sysoiev, D.; Turnhoff, S. K.; Oppermann, A.; Huhn, T.; Richtering, W.; Wöll, D. Nanoscopic Visualization of Cross-Linking Density in Polymer Networks with Diarylethene Photoswitches. *Angew. Chemie - Int. Ed.* **2018**, *57* (38), 12280–12284.

(17)   Wöll, D.; Flors, C. Super-Resolution Fluorescence Imaging for Materials Science. *Small Methods* **2017**, *1*, 1700191.

(18)   Karanastasis, A. A.; Zhang, Y.; Kenath, G. S.; Lessard, M. D.; Bewersdorf, J.; Ullal, C. K. 3D Mapping of Nanoscale Crosslink Heterogeneities in Microgels. *Mater. Horizons* **2018**, 1130–1136.

(19)   Aoki, H.; Mori, K.; Ito, S. Conformational Analysis of Single Polymer Chains in Three Dimensions by Super-Resolution Fluorescence Microscopy. *Soft Matter* **2012**, *8* (16), 4390–4395.

(20)   Albertazzi, L.; van der Zwaag, D.; Leenders, C. M. a; Fitzner, R.; van der Hofstad, R. W.; Meijer, E. W. Probing Exchange

Pathways in One-Dimensional Aggregates with Super-Resolution Microscopy. *Science* **2014**, *344* (6183), 491–495.

(21) Harke, B.; Ullal, C. K.; Keller, J.; Hell, S. W. Three-Dimensional Nanoscopy of Colloidal Crystals. *Nano Lett.* **2008**, *8* (5), 1309–1313.

(22) Ullal, C. K.; Schmidt, R.; Hell, S. W.; Egner, A. Block Copolymer Nanostructures Mapped by Far-Field Optics. *Nano Lett.* **2009**, *9* (6), 2497–2500.

(23) Boott, C. E.; Laine, R. F.; Mahou, P.; Finnegan, J. R.; Leitao, E. M.; Webb, S. E. D.; Kaminski, C. F.; Manners, I. In Situ Visualization of Block Copolymer Self-Assembly in Organic Media by Super-Resolution Fluorescence Microscopy. *Chem. - A Eur. J.* **2015**, 18539–18542.

(24) Urban, B. E.; Dong, B.; Nguyen, T.-Q.; Backman, V.; Sun, C.; Zhang, H. F. Subsurface Super-Resolution Imaging of Unstained Polymer Nanostructures. *Sci. Rep.* **2016**, *6*, 28156.

(25) Böhmer, M.; Enderlein, J. Orientation Imaging of Single Molecules by Wide-Field Epifluorescence Microscopy. *J. Opt. Soc. Am. B* **2003**, *20*, 554–559.

(26) Mortensen, K. I.; Churchman, L. S.; Spudich, J. A.; Flyvbjerg, H. Optimized Localization Analysis for Single-Molecule Tracking and Super-Resolution Microscopy. *Nat. Methods* **2010**, *7* (5), 377–381.

(27) Backlund, M. P.; Lew, M. D.; Backer, a. S.; Sahl, S. J.; Grover, G.; Agrawal, A.; Piestun, R.; Moerner, W. E. Simultaneous, Accurate Measurement of the 3D Position and Orientation of Single Molecules. *Proc. Natl. Acad. Sci.* **2012**, *109* (47), 19087–19092.

(28) Huang, B.; Wang, W.; Bates, M.; Zhuang, X. Three-Dimensional Super-Resolution Imaging by Stochastic Optical Reconstruction Microscopy. *Science* **2008**, *319* (5864), 810–813.

(29) Pavani, S. R. P.; Thompson, M. A.; Biteen, J. S.; Lord, S. J.; Liu, N.; Twieg, R. J.; Piestun, R.; Moerner, W. E. Three-Dimensional, Single-Molecule Fluorescence Imaging beyond the Diffraction Limit by Using a Double-Helix Point Spread Function. *Proc. Natl. Acad. Sci. U. S. A.* **2009**, *106* (9), 2995–2999.

(30) Holtzer, L.; Meckel, T.; Schmidt, T. Nanometric Three-Dimensional Tracking Individual Quantum Dots in Cells. *Appl. Phys. Lett.* **2007**, *90*, 053902.

(31) Dong, B.; Almassalha, L.; Urban, B. E.; Nguyen, T.-Q.; Khuon, S.; Chew, T.-L.; Backman, V.; Sun, C.; Zhang, H. F. Super-Resolution Spectroscopic Microscopy via Photon Localization. *Nat. Commun.* **2016**, *7*, 12290.

(32) Zhang, Z.; Kenny, S. J.; Hauser, M.; Li, W.; Xu, K. Ultrahigh-Throughput Single-Molecule Spectroscopy and Spectrally Resolved Super-Resolution Microscopy. *Nat. Methods* **2015**, *12* (10), 935–938.

(33) Fourkas, J. T. Rapid Determination of the Three-Dimensional Orientation of Single Molecules. *Opt. Lett.* **2001**, *26* (4), 211.

(34) Engelhardt, J.; Keller, J.; Hoyer, P.; Reuss, M.; Staudt, T.; Hell, S. W. Molecular Orientation Affects Localization Accuracy in Superresolution Far-Field Fluorescence Microscopy. *Nano Lett.* **2011**, *11* (1), 209–213.

(35) Lew, M. D.; Backlund, M. P.; Moerner, W. E. Rotational Mobility of Single Molecules Affects Localization Accuracy in Super-Resolution Fluorescence Microscopy. *Nano Lett.* **2013**, *13* (9), 3967–3972.

(36) Paeng, K.; Lee, H. N.; Swallen, S. F.; Ediger, M. D. Temperature-Ramping Measurement of Dye Reorientation to Probe Molecular Motion in Polymer Glasses. *J. Chem. Phys.* **2011**, *134* (2).

(37) Forkey, J. N.; Quinlan, M. E.; Shaw, M. A.; Corrie, J. E.; Goldman, Y. E. Three-Dimensional Structural Dynamics of Myosin V by Single-Molecule Fluorescence Polarization. *Nature* **2003**, *422* (6930), 399–404.

(38) Krause, S.; Neumann, M.; Fröbe, M.; Magerle, R.; von Borczyskowski, C. Monitoring Nanoscale Deformations in a Drawn Polymer Melt with Single-Molecule Fluorescence Polarization Microscopy. *ACS Nano* **2016**, *10*, 1908–1917.

(39) Aguet, F.; Geissbühler, S.; Märki, I.; Lasser, T.; Unser, M. Super-Resolution Orientation Estimation and Localization of Fluorescent Dipoles Using 3-D Steerable Filters. *Opt. Express* **2009**, *17* (8), 6829–6848.

(40) Chou, S. Y.; Krauss, P. R.; Renstrom, P. J. Imprint Lithography with 25-Nanometer Resolution. *Science* **1996**, *272* (5258), 85–87.

(41) Wang, J.; Sun, X.; Chen, L.; Zhuang, L.; Chou, S. Y. Molecular Alignment in Submicron Patterned Polymer Matrix Using Nanoimprint Lithography. *Appl. Phys. Lett.* **2000**, *77* (2), 166.

(42) Deschout, H.; Cella Zanacchi, F.; Mlodzianoski, M.; Diaspro, A.; Bewersdorf, J.; Hess, S. T.; Braeckmans, K. Precisely and Accurately Localizing Single Emitters in Fluorescence Microscopy. *Nat. Methods* **2014**, *11* (3), 253–266.

(43) Copeland, C. R.; McGray, C. D.; Geist, J.; Aksyuk, V. A.; Liddle, J. A.; Ilic, B. R.; Stavis, S. M. Subnanometer Localization Accuracy in Widefield Optical Microscopy. *arXiv* **2017**, 1710.09803.

(44) Novotny, L.; Beversluis, M. R.; Youngworth, K. S.; Brown, T. G. Longitudinal Field Modes Probed by Single Molecules. *Phys. Rev. Lett.* **2001**, *86* (23), 5251–5254.

(45) Novotny, L.; Hecht, B. *Principles of Nano-Optics*, 2nd ed.; Cambridge University Press: Cambridge, 2012.

(46) Ding, Y.; Ro, H. W.; Douglas, J. F.; Jones, R. L.; Hine, D. R.; Karim, A.; Soles, C. L. Polymer Viscoelasticity and Residual Stress Effects on Nanoimprint Lithography. *Adv. Mater.* **2007**, *19* (10), 1377–1382.

(47) Davis, D. A.; Hamilton, A.; Yang, J.; Cremar, L. D.; Van Gough, D.; Potisek, S. L.; Ong, M. T.; Braun, P. V; Martinez, T. J.; White, S. R.; Moore, J. S.; Sottos, N. R. Force-Induced Activation of Covalent Bonds in Mechanoresponsive Polymeric Materials. *Nature* **2009**, *459*, 68–72.

(48) Ducrot, E.; Chen, Y.; Bulters, M.; Sijbesma, R. P.; Creton, C. Toughening Elastomers with Sacrificial Bonds and Watching Them Break. *Science* **2014**, *344* (April), 186–190.

(49) Smith, C. S.; Joseph, N.; Rieger, B.; Lidke, K. A. Fast, Single-Molecule Localization That Achieves Theoretically Minimum Uncertainty. *Nat. Methods* **2010**, *7* (5), 373–375.

(50) Huang, F.; Schwartz, S. L.; Byars, J. M.; Lidke, K. A. Simultaneous Multiple-Emitter Fitting for Single Molecule Super-Resolution Imaging. *Biomed. Opt. Express* **2011**, *2*, 1377–1393.

(51) Yang, J. K. W.; Berggren, K. K. Using High-Contrast Salty Development of Hydrogen Silsesquioxane for Sub-10-Nm Half-Pitch Lithography. *J. Vac. Sci. Technol. B* **2007**, *25*, 2025–2029.

(52) Balram, K. C.; Westly, D. A.; Davanço, M.; Grutter, K. E.; Li, Q.; Czaplewski, D. A.; Ocola, L.; Srinivasan, K. A.; Stavis, S. M. The Nanolithography Toolbox. *J. Res. Natl. Inst. Stand. Technol.* **2016**, *121*, 464–475.